Supporting Information

Rational Designed Two-Dimensional $MoSe_2/Ti_2CO_2$ Heterojunction for Photocatalytic Overall Water Splitting: Simultaneously Suppressing Electron-Hole Recombination and Photocorrosion

Cen-Feng Fu, Xingxing Li, and Jinlong Yang*

Hefei National Laboratory of Physical Science at the Microscale, Department of Chemical Physics, Synergetic Innovation Center of Quantum Information & Quantum Physics, University of Science and Technology of China, Anhui 230026, China

E-mail: jlyang@ustc.edu.cn

Computational Methods and Details

Density Functional Theory Calculations

All the density functional theory (DFT) calculations are performed by using the Vienna *ab initio* simulation package (VASP).[1,2] The interaction between the core and valence electrons is described using the frozen-core projector augmented wave approach.[3,4] The generalized gradient approximation of Perdew-Burke-Ernzerhof (PBE)[5] functional is employed. To obtain accurate electronic structures, the Heyd-Scuseria-Ernzerhof (HSE06)[6] hybrid functional is used. The energy cutoff is set to be 500 eV. A Γ-centered mesh of $5 \times 5 \times 1$ and $3 \times 3 \times 1$ k-points is used to sample the two-dimensional Brillouin zone for PBE and HSE06 calculations, respectively. The DFT-D2 method proposed by Grimme is adopted to describe long-range vdW interactions.[7] A vacuum space greater than 20 Å vertical to the sheet is applied to separate the interactions between neighboring slabs. Dipole correction is employed due to the asymmetric layer arrangement. All geometry structures are fully relaxed until the convergence criteria of energy and force are less than 10^{-5} eV and 0.02 eV Å^{-1}, respectively.

Free Energy Changes for OER

The free energy differences (ΔG) for the OER are calculated according to the approach originally proposed by Nørskov and coworkers:[8,9]

$$\Delta G = \Delta E + \Delta E_{zpe} - T\Delta S - \Delta G_{pH} + \Delta G_U$$

where ΔE is the computed reaction energy, ΔE_{zpe} and ΔS are the zero-point energy difference and the entropy difference between the absorbed state and gas phase,[9] respectively, and T (set to 298.15 K) is the system temperature. The pH dependence of the redox potential is considered by $\Delta G_{pH} = 0.059 \times \text{pH}$, which originates from the H^+ concentration dependence of the entropy.[9] The external potential supplied by photo-generated holes is added by

$\Delta G_U = -eU_h$, where U_h is the electrode potential relative to the standard hydrogen electrode (seen in **Figure 2 (a)**). The details for evaluating the ΔG for the OER are described in the following content.

The OER is a reaction process involved in four electrons, which can be written as:[8,9]

$$\mathrm{A}: \quad * + \mathrm{H_2O} \rightarrow *\mathrm{OH} + \mathrm{H^+} + \mathrm{e^-} \tag{1}$$

$$\mathrm{B}: \quad *\mathrm{OH} \rightarrow *\mathrm{O} + \mathrm{H^+} + \mathrm{e^-} \tag{2}$$

$$\mathrm{C}: \quad *\mathrm{O} + \mathrm{H_2O} \rightarrow *\mathrm{OOH} + \mathrm{H^+} + \mathrm{e^-} \tag{3}$$

$$\mathrm{D}: \quad *\mathrm{OOH} \rightarrow * + \mathrm{O_2} + \mathrm{H^+} + \mathrm{e^-} \tag{4}$$

where * denotes the adsorption site, *OH, *O and *OOH denote the adsorbed intermediate states. Then, considering the contribution from the zero-point energy, the entropy, the pH dependence of the redox potential, and the external potential supplied by the photogenerated holes, the free energy changes along the OER pathway can be expressed as:[8,9]

$$\Delta G_\mathrm{A} = G_{*\mathrm{OH}} + \frac{1}{2}G_{\mathrm{H_2}} - G_* - G_{\mathrm{H_2O}} - \Delta G_{pH} - eU_h \tag{5}$$

$$\Delta G_\mathrm{B} = G_{*\mathrm{O}} + \frac{1}{2}G_{\mathrm{H_2}} - G_{*\mathrm{OH}} - \Delta G_{pH} - eU_h \tag{6}$$

$$\Delta G_\mathrm{C} = G_{*\mathrm{OOH}} + \frac{1}{2}G_{\mathrm{H_2}} - G_{*\mathrm{O}} - G_{\mathrm{H_2O}} - \Delta G_{pH} - eU_h \tag{7}$$

$$\Delta G_\mathrm{D} = G_* + \frac{1}{2}G_{\mathrm{H_2}} + G_{\mathrm{O_2}} - G_{*\mathrm{OOH}} - \Delta G_{pH} - eU_h \tag{8}$$

Herein, various intermediate states along the reaction paths are calculated based on the consideration of the absorption of free radicals or atoms on the material surface, and $\frac{1}{2}G_{\mathrm{H_2}}$ represent the Gibbs free energy of $\mathrm{H^+} + \mathrm{e^-}$ at the standard conditions of pressure and temperature. The pH dependence of the redox potential is considered by $\Delta G_{pH} = 0.059 \times pH$. The entropy of the free molecules ($\mathrm{O_2}$, $\mathrm{H_2}$, and $\mathrm{H_2O}$) are taken from the NIST database.

The free energy of O_2(g) is derived as:

$$G_{O_2} = 2G_{H_2O} - 2G_{H_2} - 4.92 \text{ eV} \tag{9}$$

The zero point energy term is given as:[9]

$$E_{zpe} = \sum_i \frac{1}{2} h\nu_i \tag{10}$$

and the entropy is obtained as:[9]

$$S_{vib} = R \sum_i \left\{ \frac{h\nu_i / k_B T}{\exp\left(\frac{h\nu_i}{k_B T}\right) - 1} - \ln\left[1 - \exp\left(-\frac{h\nu_i}{k_B T}\right)\right] \right\} \tag{11}$$

where h is Planck's constant, ν is the vibrational frequency, R is the gas constant, T is the absolute temperature and k_B is Boltzmann's constant.

For the OER involving the surface lattice O (O_L) of Ti_2CO_2, the four-electron reactions are:

$$\text{E}: \quad O_L + H_2O \rightarrow *OOH + H^+ + e^- \tag{12}$$

$$\text{F}: \quad *OOH \rightarrow V_O + O_2 + H^+ + e^- \tag{13}$$

$$\text{G}: \quad V_O + H_2O \rightarrow *OH + H^+ + e^- \tag{14}$$

$$\text{H}: \quad *OH \rightarrow O_L + H^+ + e^- \tag{15}$$

where O_L and V_O denote the surface lattice O and O vacancy, respectively, *OOH and *OH denote the adsorbed intermediate states. Similar to the normal OER process, the free energy

changes along the reaction pathway can be expressed as:

$$\Delta G_{\mathrm{E}} = G_{*\mathrm{OOH}} + \frac{1}{2}G_{\mathrm{H_2}} - G_{\mathrm{O_L}} - G_{\mathrm{H_2O}} - \Delta G_{pH} - eU_h \tag{16}$$

$$\Delta G_{\mathrm{F}} = G_{\mathrm{V_O}} + \frac{1}{2}G_{\mathrm{H_2}} + G_{\mathrm{O_2}} - G_{*\mathrm{OOH}} - \Delta G_{pH} - eU_h \tag{17}$$

$$\Delta G_{\mathrm{G}} = G_{*\mathrm{OH}} + \frac{1}{2}G_{\mathrm{H_2}} - G_{\mathrm{V_O}} - G_{\mathrm{H_2O}} - \Delta G_{pH} - eU_h \tag{18}$$

$$\Delta G_{\mathrm{H}} = G_{\mathrm{O_L}} + \frac{1}{2}G_{\mathrm{H_2}} - G_{*\mathrm{OH}} - \Delta G_{pH} - eU_h \tag{19}$$

Non-adiabatic molecular dynamics simulations

The *ab initio* non-adiabatic molecular dynamics (NAMD) calculations are implemented within the framework of time dependent Kohn-Sham (TDKS) equation combined with surface hopping scheme. The simulations are carried out using Hefei-NAMD code,[10–14] which augments the VASP with the NAMD capabilities. The wave functions are calculated by the PBE functional with the addition of on-site Hubbard U (= 4.2 eV)[15] repulsion on the Ti $3d$ orbitals. After geometry optimization, the system is heated and equalized at 300 K by using the velocity rescaling method for 13 ps. Then, a 2 ps *ab initio* molecular dynamics (MD) trajectory is generated at the Γ point in the microcanonical ensemble with a time step of 1 fs. The NAMD results are based on average over 200 different initial configurations obtained from the MD trajectory. For each chosen structure, we sample 2×10^4 trajectories for the next 0.5 ps.

Calculation of the Solar-to-Hydrogen Efficiency

According to the previous work,[16,17] the efficiency upper limits of the solar-to-hydrogen (STH) are predicted by:

$$\eta_{STH} = 0.5 \times \frac{\Delta G \int_E^\infty \frac{P(h\omega)}{h\omega} d(h\omega)}{\int_0^\infty P(h\omega) d(h\omega)} \tag{20}$$

where $P(h\omega)$ is the AM1.5G solar energy flux at the photon energy $h\omega$, ΔG is the potential difference of 1.23 eV for water splitting, and E is the energy of photons that can actually be

utilized for water splitting. The integral from 0 to ∞ in the denominator represents the total power density of incident simulative sunlight (AM1.5G), while the integral from E to ∞ in the numerator is the effective photocurrent density. Determining the extra energy needed to overcome the barriers of the HER and OER is important for calculating STH efficiency. Because the OER can process spontaneously under light irradiation and the U_e is large enough to drive the HER, we assume that all the photo-generated carriers will be converted to hydrogen, namely, E is equal to E_g (band gap) for the $MoSe_2/Ti_2CO_2$ heterojunction and the catalytic reaction efficiency is 100%. The 0.5 denotes that only half of the photo-generated carriers can be converted to hydrogen energy in Z-scheme photocatalytic water splitting.

Calculation of the Optical Absorption Spectra

The optical absorption spectra are simulated by converting the complex dielectric function to the absorption coefficient $\alpha_{abs}(\omega)$ according to the relation:[18]

$$\alpha_{abs}(\omega) = \sqrt{2}\omega\sqrt{\sqrt{\varepsilon_1^2(\omega) + \varepsilon_2^2(\omega)} - \varepsilon_1(\omega)} \tag{21}$$

where $\varepsilon_1(\omega)$ and $\varepsilon_2(\omega)$ are the real and imaginary parts of frequency-dependent complex dielectric function $\varepsilon(\omega)$, respectively. Due to the tensor nature of the dielectric function, $\varepsilon_1(\omega)$ and $\varepsilon_2(\omega)$ are averaged over three polarization vectors (along x-, y- and z-directions).

Structural, Electronic and Free Energy Results

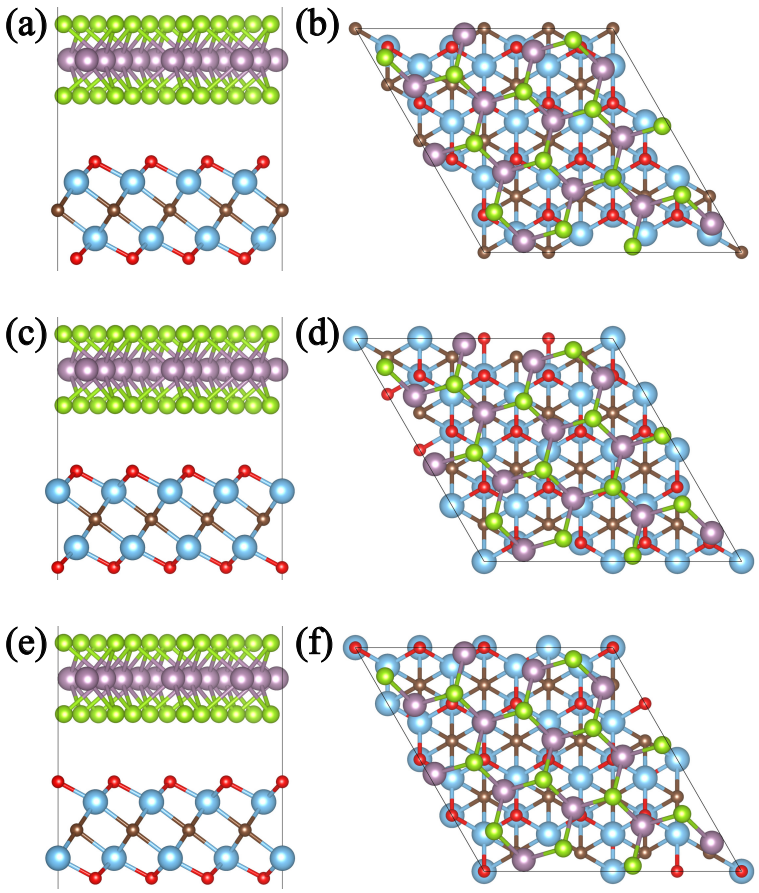

Figure S1. The configurations for the $MoSe_2/Ti_2CO_2$ heterojunction with different stacking patterns of the A1 (a, b), A2 (c, d) and A3 (e, f). The Mo, Se, Ti, C and O atoms are represented as purple, green, cyan, brown and red balls, respectively.

We have examined the effect of different stacking patterns on the binding energy and vertical distance between the two components of the two-dimensional (2D) van der Waals (vdW) $MoSe_2/Ti_2CO_2$ heterojunction. Three different stacking structures are chosen (presented in **Figure S1**), and the binding energies and vertical distances between the $MoSe_2$ and Ti_2CO_2 monolayers are listed in **Table S1**. The differences of both the binding energies and vertical distances between the $MoSe_2$ and Ti_2CO_2 monolayers are very small. Thus,

the effect of the different stacking patterns on the binding energies and vertical distances between the two components of the 2D vdW $MoSe_2/Ti_2CO_2$ heterojunction is negligible. Due to the largest binding energy among the different configurations, the A1 configuration is chosen for the calculations of the electronic properties and free energy variations.

Table S1. The binding energy and vertical separation between the two components of 2D vdW $MoSe_2/Ti_2CO_2$ heterojunction with different stacking patterns.

Configuration	Binding energy (meV/atom)	Vertical separation (Å)
A1	−16.8	3.07
A2	−16.7	3.07
A3	−16.6	3.15

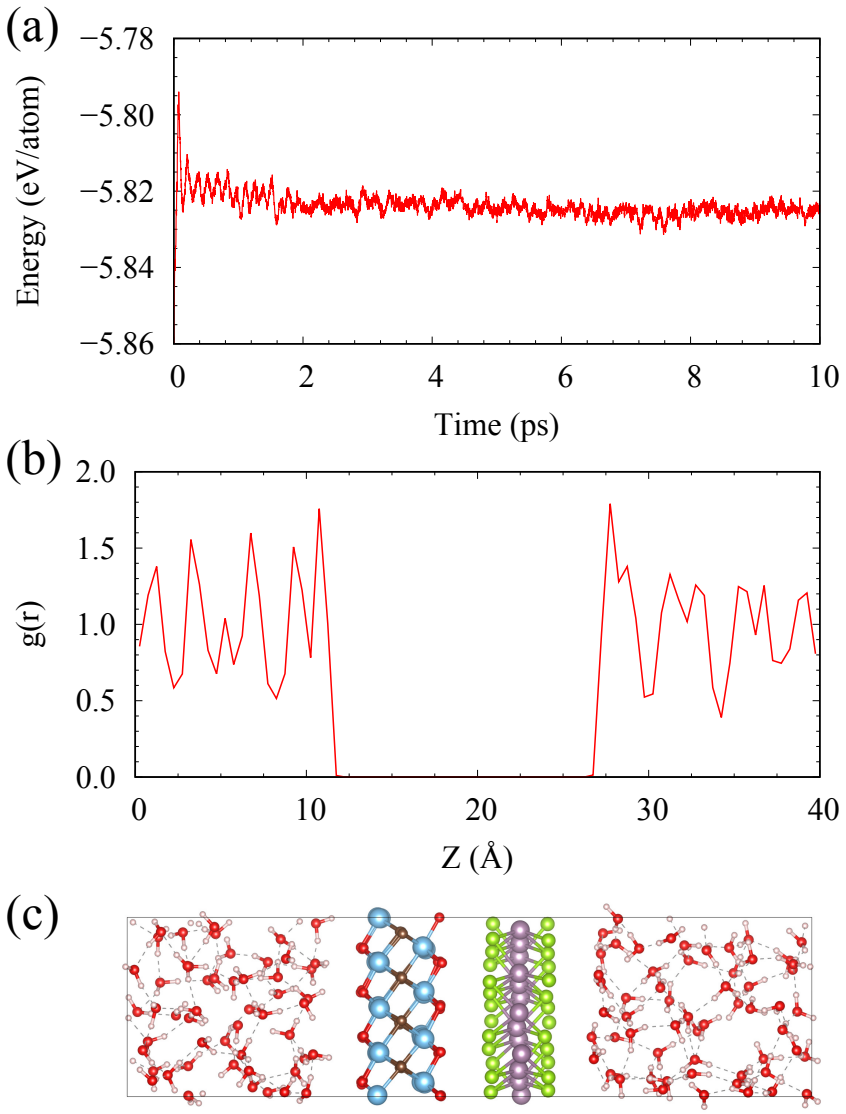

Figure S2. (a) Evolution of the total energy of *ab initio* molecular dynamics for the $MoSe_2/Ti_2CO_2$ heterojunction in liquid water at 300 K. (b) Normalized distribution function g(r) of O atom in water along z axis for the last 5.0 ps simulation. (c) Snapshot structure of the the $MoSe_2/Ti_2CO_2$ heterojunction in liquid water.

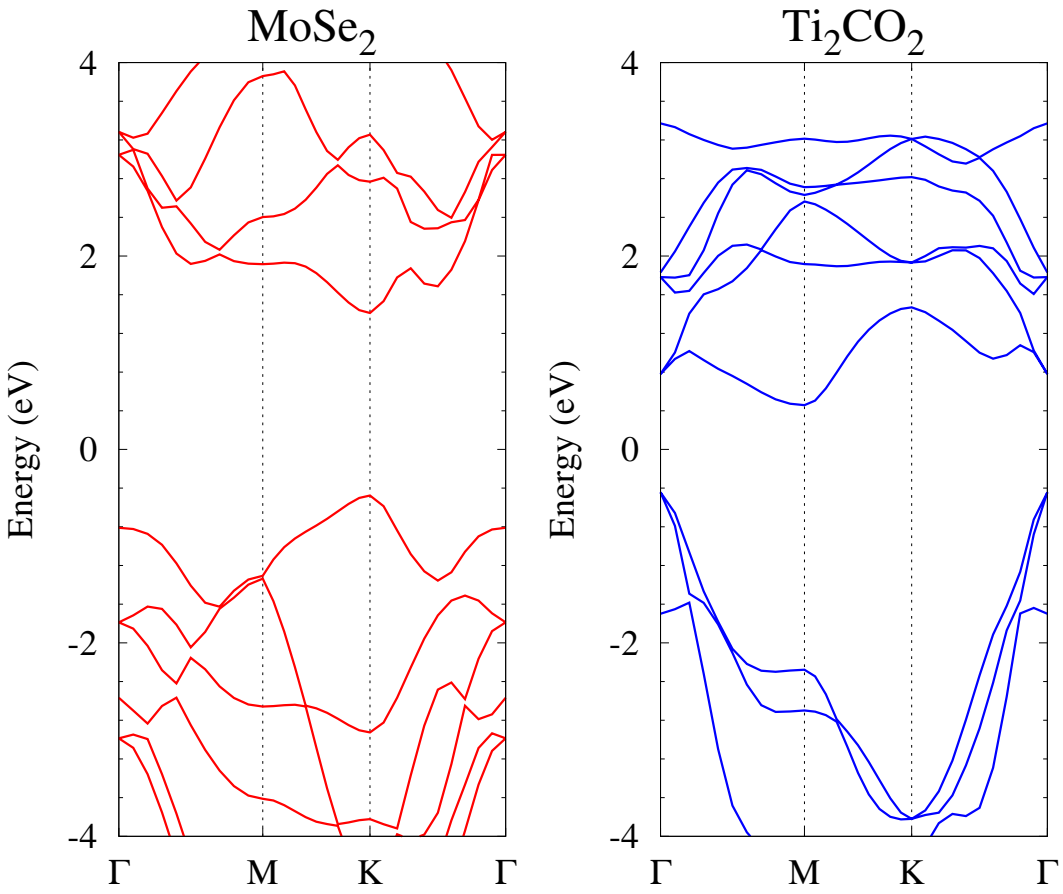

Figure S3. Band structures of the $MoSe_2$ and Ti_2CO_2 monolayers calculated by HSE06 hybrid functional. The Fermi levels are set to zero.

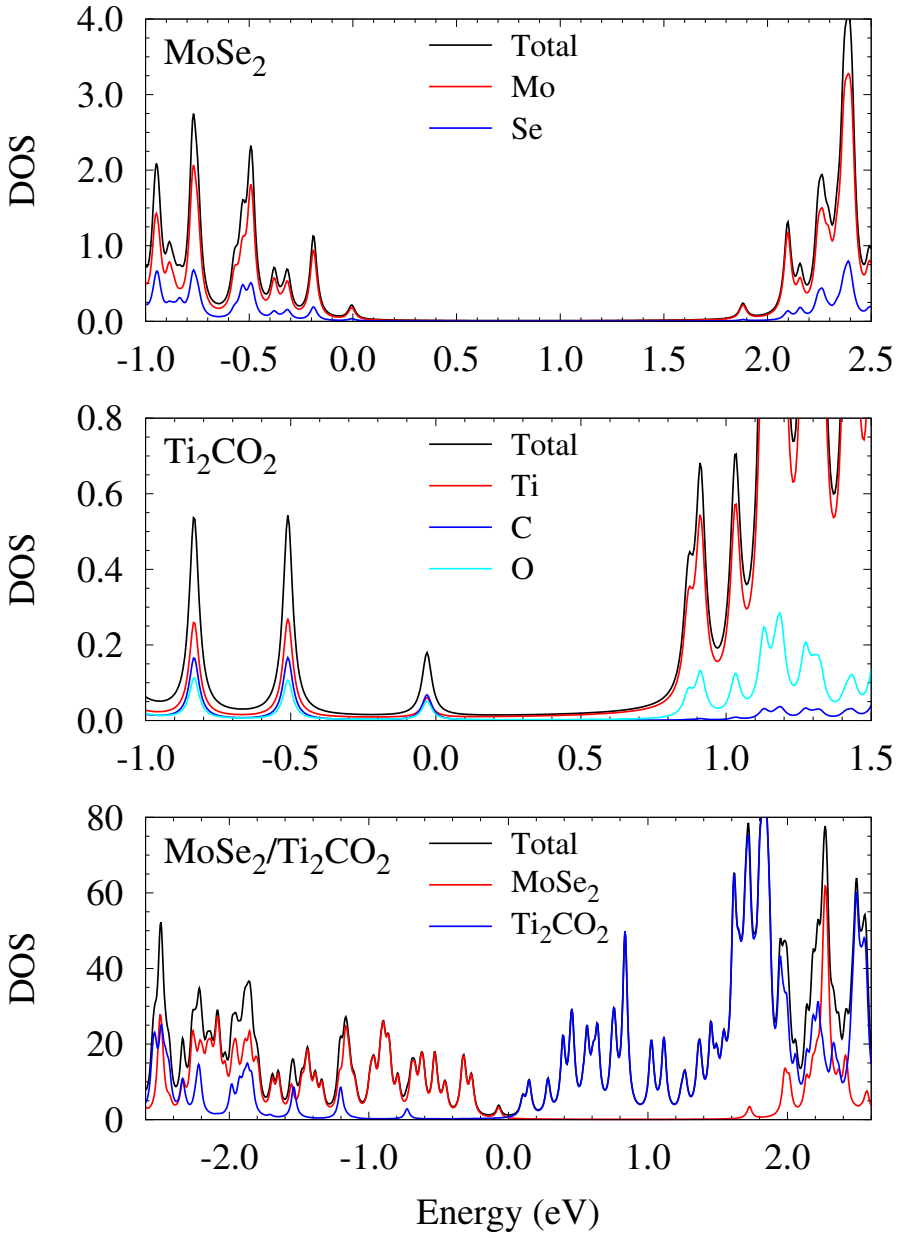

Figure S4. Total DOS and projected DOS for free-standing $MoSe_2$ and Ti_2CO_2 monolayers as well as the $MoSe_2/Ti_2CO_2$ heterojunction.

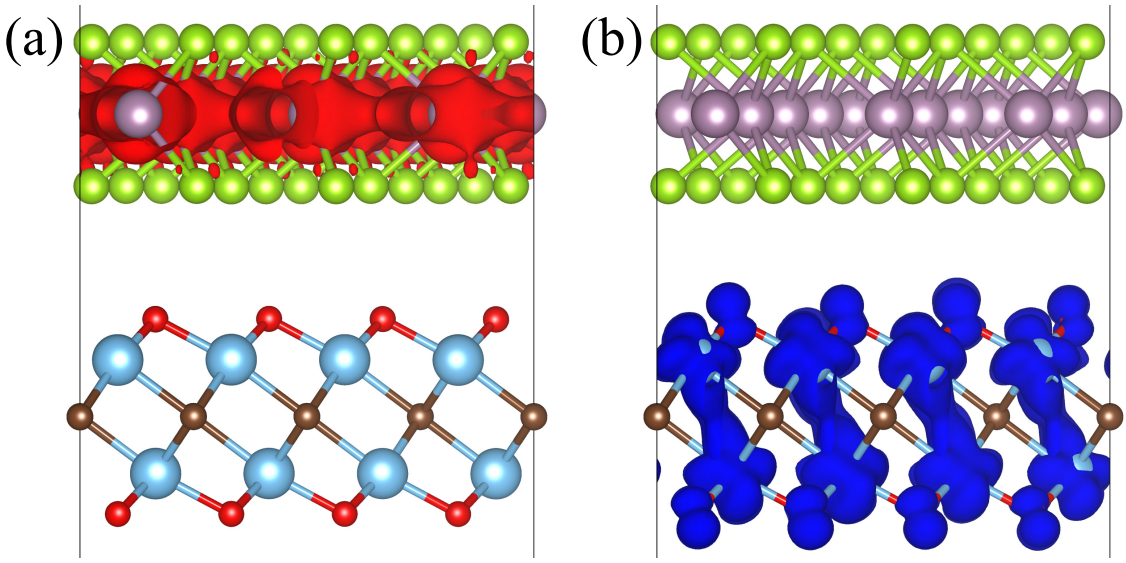

Figure S5. Spatial distribution of the valence band (a) and conduction band (b) for the $MoSe_2/Ti_2CO_2$ heterojunction. The red and blue regions indicate the distribution of the valence band and conduction band, respectively.

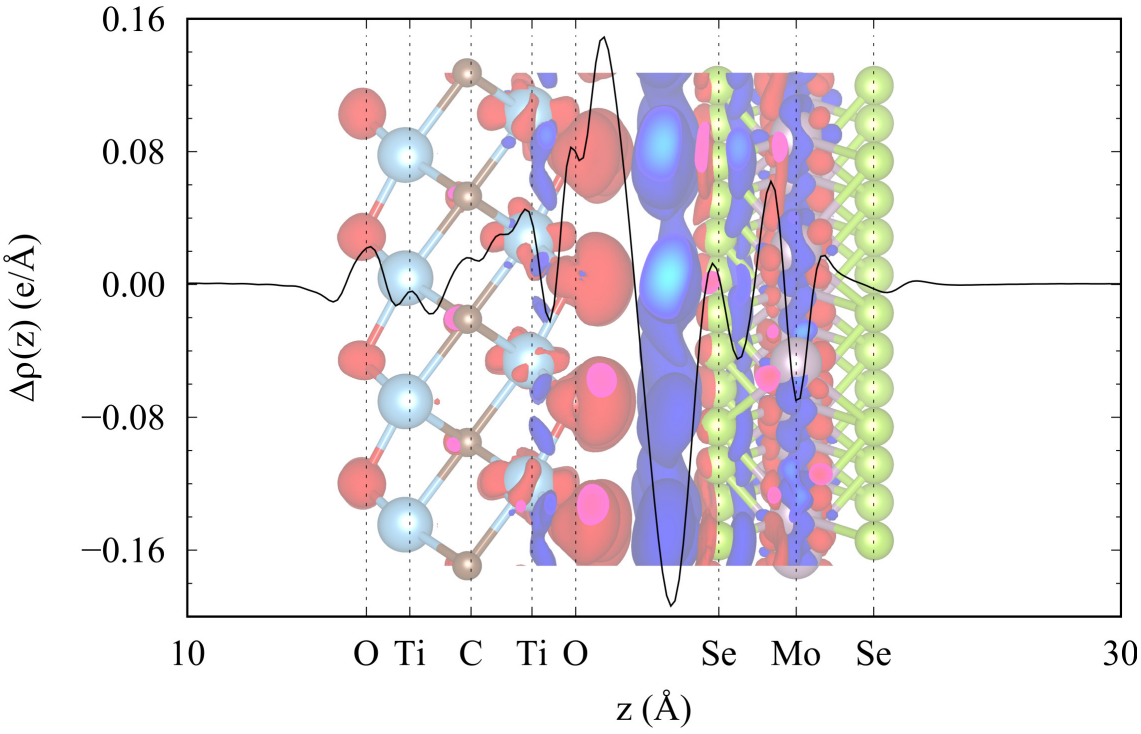

Figure S6. The plane-integrated electron density difference along the vertical direction of the $MoSe_2/Ti_2CO_2$ heterojunction. The background represents the charge redistribution with the red and blue regions presenting the electron accumulation and depletion, respectively.

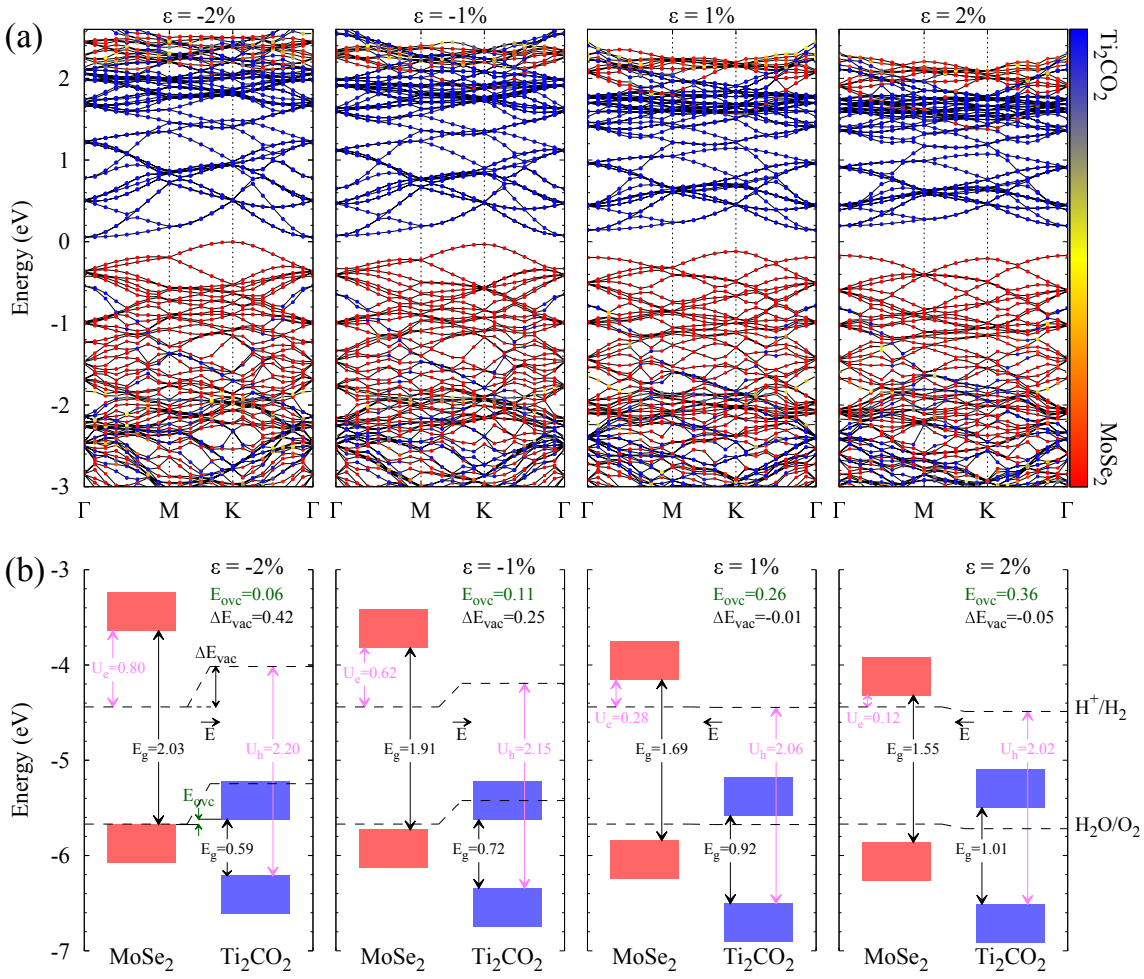

Figure S7. Biaxial strain effect on the band structure (a) as well as band edge alignment (b) of the $MoSe_2/Ti_2CO_2$ heterojunction. The circles with color from red to blue in (a) represent the dominated contributions varying from $MoSe_2$ to Ti_2CO_2. The values in (b) are all in eV.

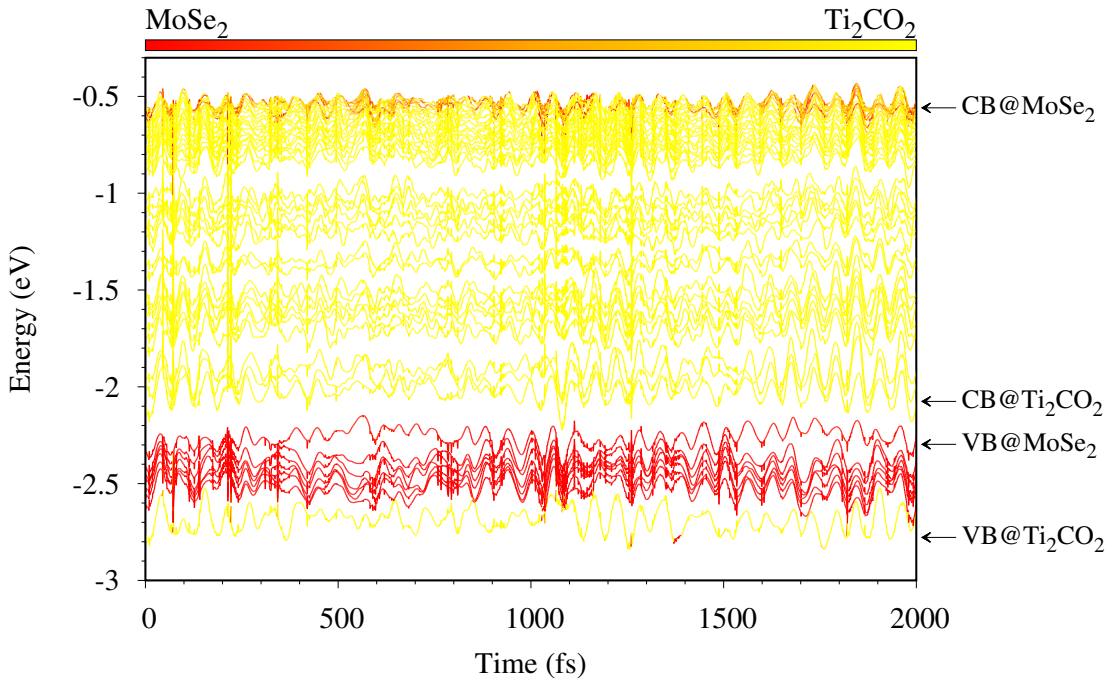

Figure S8. Time-dependent evolutions of the energy states for the nonadiabatic molecular dynamics simulations. The color bar suggests the contribution of $MoSe_2$ and Ti_2CO_2 to each band. VB@$MoSe_2$, VB@Ti_2CO_2, CB@$MoSe_2$ and CB@Ti_2CO_2 represent the valence band (VB) and conduction band (CB) of $MoSe_2$ and Ti_2CO_2.

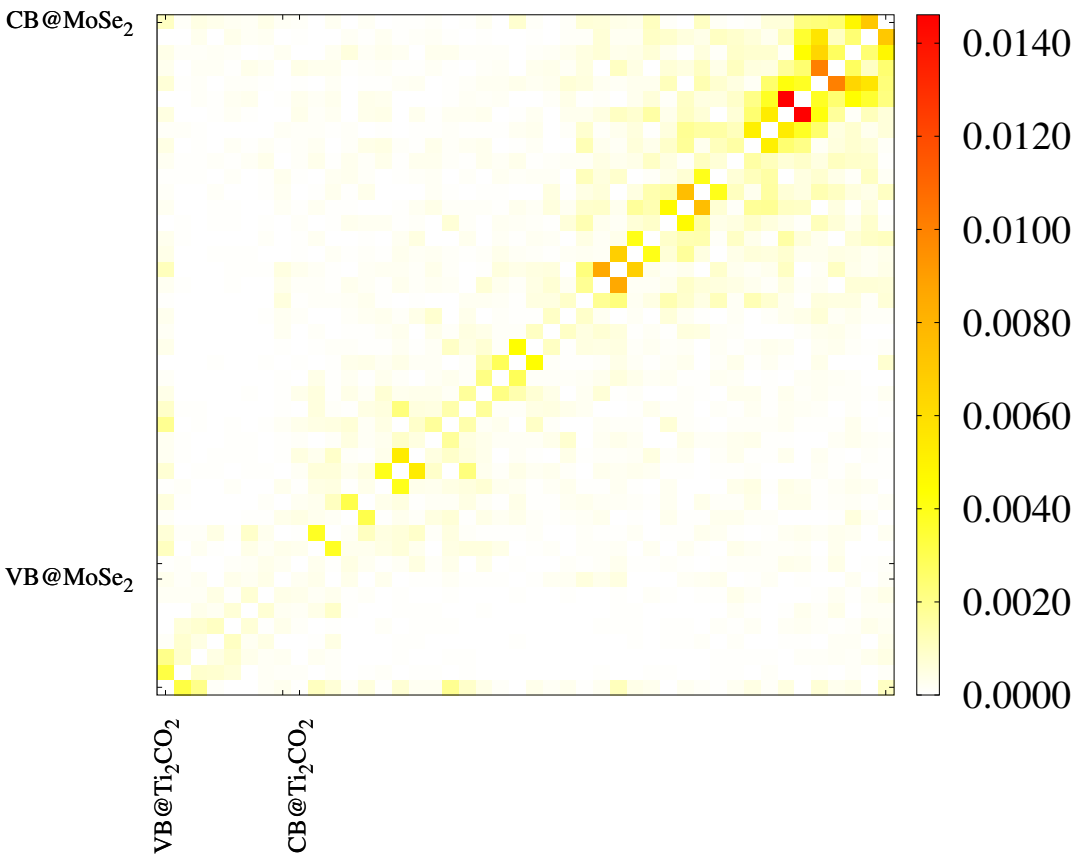

Figure S9. The averaged values of nonadiabatic coupling between different states. VB@$MoSe_2$, VB@Ti_2CO_2, CB@$MoSe_2$ and CB@Ti_2CO_2 represent the valence band (VB) and conduction band (CB) of $MoSe_2$ and Ti_2CO_2.

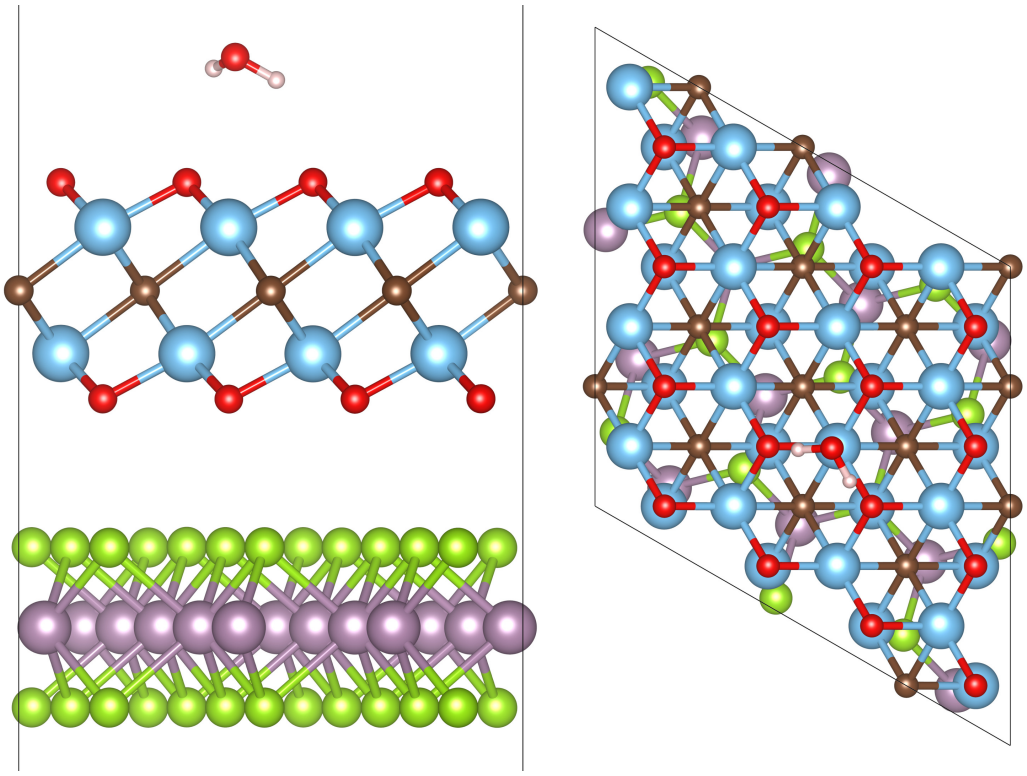

Figure S10. Side and top views of the most stable absorption structures of H_2O molecule on the Ti_2CO_2 surface.

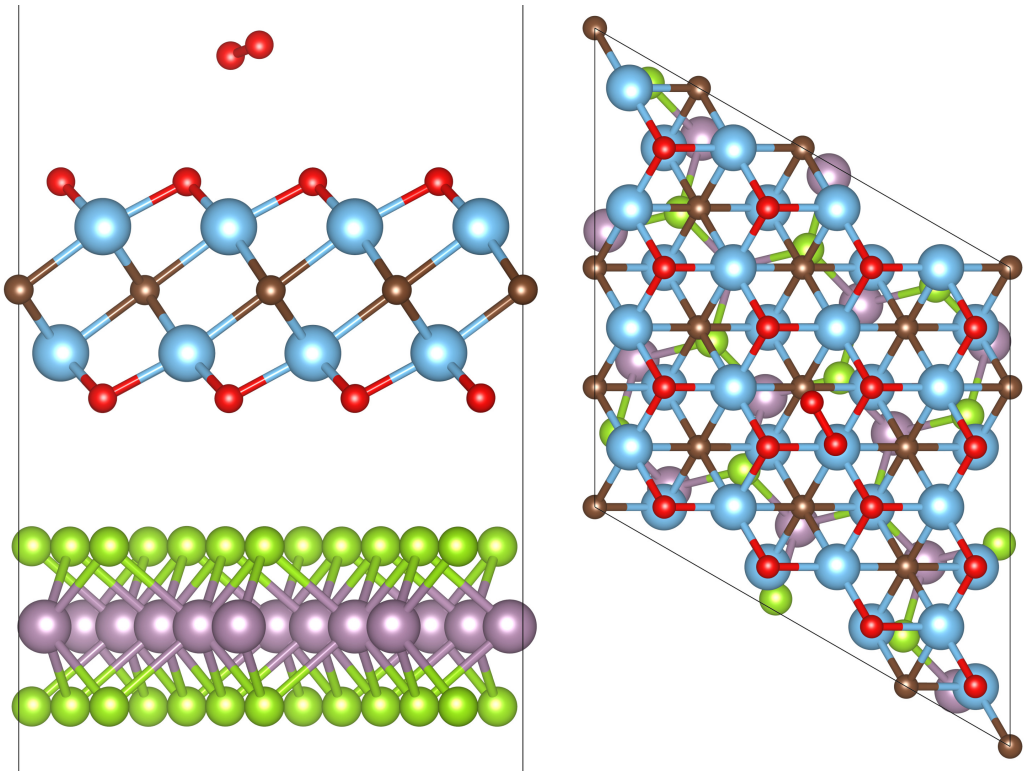

Figure S11. Side and top views of the most stable absorption structures of O_2 molecule on the Ti_2CO_2 surface.

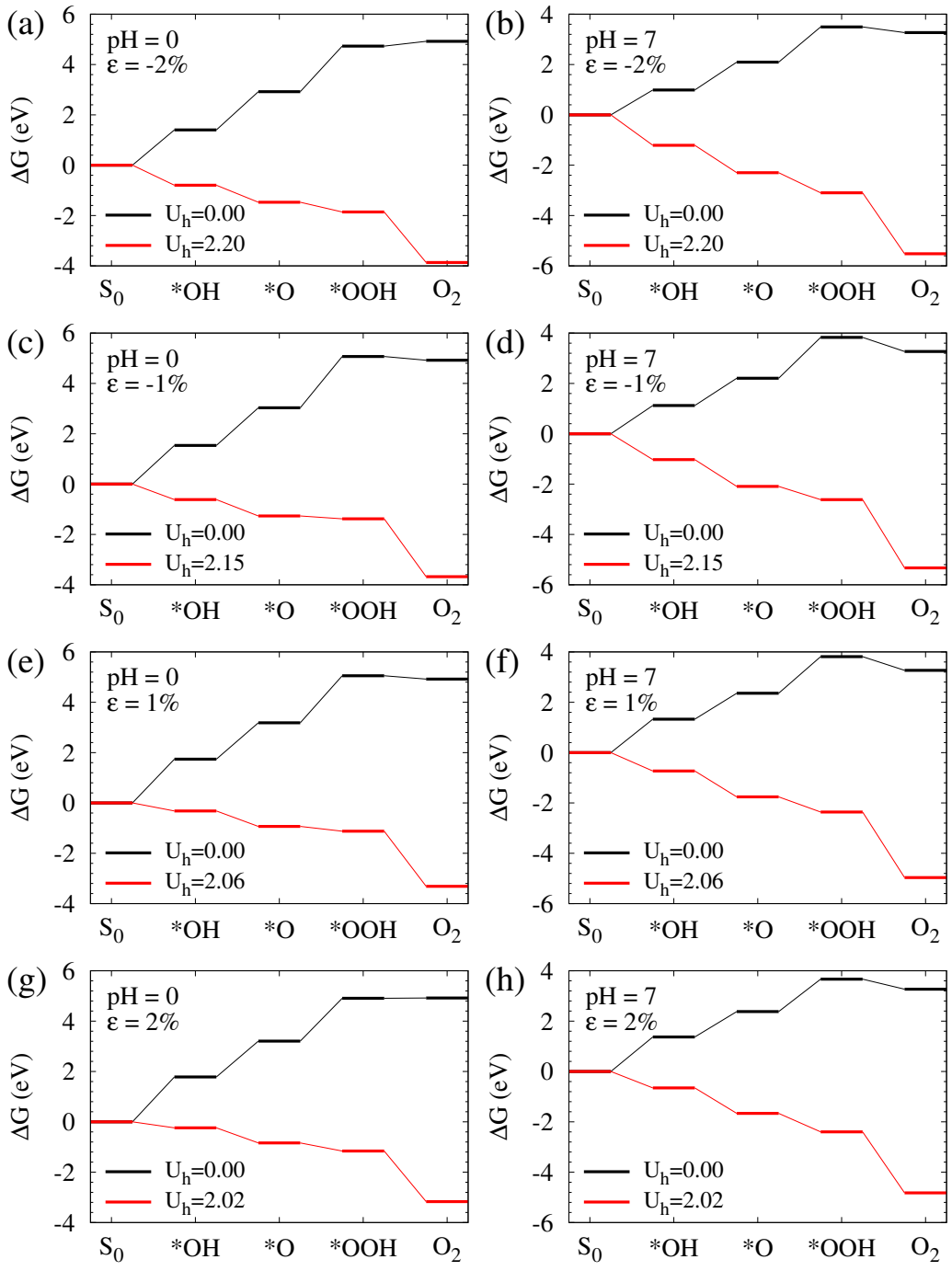

Figure S12. Free energy diagrams for the oxygen evolution reaction on the Ti_2CO_2 surface at pH = 0 (a,c,e) and pH = 7 (b,d,f) under biaxial strain.

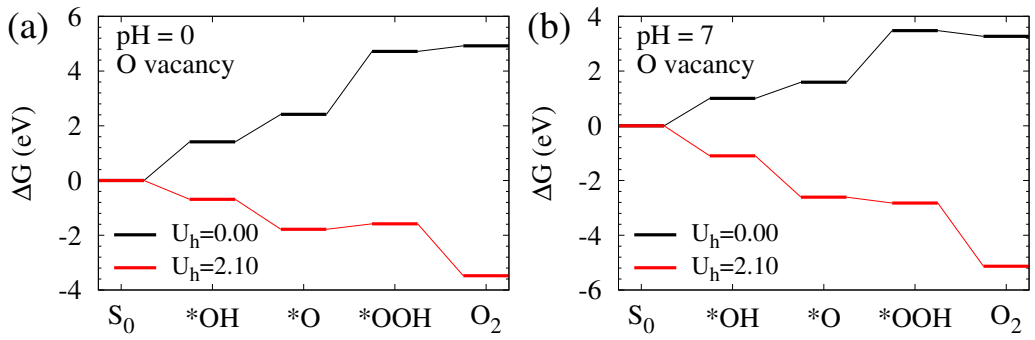

Figure S13. Free energy diagrams for the oxygen evolution reaction with O vacancy on the Ti_2CO_2 surface at pH = 0 (a) and pH = 7 (b).

References

(1) Kresse, G.; Furthmüller, J. Efficient iterative schemes for ab initio total-energy calculations using a plane-wave basis set. *Phys. Rev. B* **1996**, *54*, 11169–11186.

(2) Kresse, G.; Furthmüller, J. Efficiency of ab-initio total energy calculations for metals and semiconductors using a plane-wave basis set. *Comput. Mater. Sci.* **1996**, *6*, 15–50.

(3) Blöchl, P. E. Projector augmented-wave method. *Phys. Rev. B* **1994**, *50*, 17953–17979.

(4) Kresse, G.; Joubert, D. From ultrasoft pseudopotentials to the projector augmented-wave method. *Phys. Rev. B* **1999**, *59*, 1758–1775.

(5) Perdew, J. P.; Burke, K.; Ernzerhof, M. Generalized Gradient Approximation Made Simple. *Phys. Rev. Lett.* **1996**, *77*, 3865–3868.

(6) Heyd, J.; Scuseria, G. E.; Ernzerhof, M. Hybrid functionals based on a screened Coulomb potential. *J. Chem. Phys.* **2003**, *118*, 8207–8215.

(7) Grimme, S. Semiempirical GGA-type density functional constructed with a long-range dispersion correction. *J. Comput. Chem.* **2006**, *27*, 1787–1799.

(8) Nørskov, J. K.; Rossmeisl, J.; Logadottir, A.; Lindqvist, L.; Kitchin, J. R.; Bligaard, T.; Jónsson, H. Origin of the Overpotential for Oxygen Reduction at a Fuel-Cell Cathode. *J. Phys. Chem. B* **2004**, *108*, 17886–17892.

(9) Howalt, J. G.; Bligaard, T.; Rossmeisl, J.; Vegge, T. DFT based study of transition metal nano-clusters for electrochemical NH3 production. *Phys. Chem. Chem. Phys.* **2013**, *15*, 7785–7795.

(10) Craig, C. F.; Duncan, W. R.; Prezhdo, O. V. Trajectory Surface Hopping in the Time-Dependent Kohn-Sham Approach for Electron-Nuclear Dynamics. *Phys. Rev. Lett.* **2005**, *95*, 163001.

(11) Akimov, A. V.; Prezhdo, O. V. The PYXAID Program for Non-Adiabatic Molecular Dynamics in Condensed Matter Systems. *J. Chem. Theory Comput.* **2013**, *9*, 4959–4972.

(12) Zhang, R.; Zhang, L.; Zheng, Q.; Gao, P.; Zhao, J.; Yang, J. Direct Z-Scheme Water Splitting Photocatalyst Based on Two-Dimensional Van Der Waals Heterostructures. *J. Phys. Chem. Lett.* **2018**, *9*, 5419–5424.

(13) Zheng, Q.; Chu, W.; Zhao, C.; Zhang, L.; Guo, H.; Wang, Y.; Jiang, X.; Zhao, J. Ab initio nonadiabatic molecular dynamics investigations on the excited carriers in condensed matter systems. *WIREs Comput. Mol. Sci.* **2019**, *9*, e1411.

(14) Niu, X.; Bai, X.; Zhou, Z.; Wang, J. Rational Design and Characterization of Direct Z-Scheme Photocatalyst for Overall Water Splitting from Excited State Dynamics Simulations. *ACS Catal.* **2020**, *10*, 1976–1983.

(15) Morgan, B. J.; Watson, G. W. A DFT+U description of oxygen vacancies at the TiO_2 rutile (110) surface. *Surf. Sci.* **2007**, *601*, 5034–5041.

(16) Fu, C.-F.; Sun, J.; Luo, Q.; Li, X.; Hu, W.; Yang, J. Intrinsic Electric Fields in Two-dimensional Materials Boost the Solar-to-Hydrogen Efficiency for Photocatalytic Water Splitting. *Nano Lett.* **2018**, *18*, 6312–6317.

(17) Fan, Y.; Wang, J.; Zhao, M. Spontaneous full photocatalytic water splitting on 2D $MoSe_2/SnSe_2$ and $WSe_2/SnSe_2$ vdW heterostructures. *Nanoscale* **2019**, *11*, 14836–14843.

(18) Gajdoš, M.; Hummer, K.; Kresse, G.; Furthmüller, J.; Bechstedt, F. Linear optical properties in the projector-augmented wave methodology. *Phys. Rev. B* **2006**, *73*, 045112.